Mapping Metals Incorporation of a Whole Single Catalyst Particle Using Element Specific X-ray Nanotomography

Florian Meirer,[†,§] Darius T. Morris,[‡,§] Sam Kalirai,[†] Yijin Liu,[‡] Joy C. Andrews,*[,‡] and Bert M. Weckhuysen*[,†]

[†]Department of Inorganic Chemistry and Catalysis, Debye Institute for Nanomaterials Science, Utrecht University, Utrecht, The Netherlands

[‡]Stanford Synchrotron Radiation Lightsource, SLAC National Accelerator Laboratory, Menlo Park, California 94025, United States

S Supporting Information

ABSTRACT: Full-field transmission X-ray microscopy has been used to determine the 3D structure of a whole individual fluid catalytic cracking (FCC) particle at high spatial resolution and in a fast, noninvasive manner, maintaining the full integrity of the particle. Using X-ray absorption mosaic imaging to combine multiple fields of view, computed tomography was performed to visualize the macropore structure of the catalyst and its availability for mass transport. We mapped the relative spatial distributions of Ni and Fe using multiple-energy tomography at the respective X-ray absorption K-edges and correlated these distributions with porosity and permeability of an equilibrated catalyst (E-cat) particle. Both metals were found to accumulate in outer layers of the particle, effectively decreasing porosity by clogging of pores and eventually restricting access into the FCC particle.

Fluid catalytic cracking (FCC) is the refining process for converting large and/or heavy molecules of oil feedstock into smaller and lighter hydrocarbons such as gasoline. Although the use of heavy fuel oil is more economical, gasoline yield is lower and metal content is higher than in lighter, higher quality feedstocks. Metals such as Ni and V can decrease yield by catalyzing dehydrogenation of hydrocarbons present in the feedstock, leading to increased coking of the particle[1] and thus a shift toward undesirable products. Fe from the reactor chamber and from the FCC feed is suspected to also contaminate the particle by clogging pores and restricting accessibility into active domains within the particle.[2] Understanding of these phenomena is crucial for the design of future catalysts and reactors and requires fundamental insight into the effects of metal poisoning and related changes in porosity and permeability. Therefore, in order to design and produce more efficient catalysts, their structure and chemistry must be understood at the single particle level and on multiple length scales.[3] For FCC catalysts, there have been several studies investigating the topography, morphology, and deactivation of FCC particles using various experimental techniques. However, most studies attempting to investigate the roles of metals have been limited to the surface or outer layers of the catalyst particles[4,5] or to cross sections of single particles.[6] To study catalytic activity, confocal fluorescence microscopy[7] and

integrated light and electron microscopy (iLEM)[8] have been used to probe the acidity of individual FCC particles. However, these selective staining techniques do not provide insight into the 3D morphology of FCC particles at high resolution. More recently, micro-CT has been performed on several FCC particles at lower resolution (~1 μm) studying particle morphology and giant macropores within. The study also included nanotomography of a small subsection of a single catalyst particle at ~70 nm voxel size. Tomography data was collected at a single X-ray energy, and therefore, no elemental distributions were reported.[9]

In our study, we sought to provide elemental information at a high-spatial resolution and hereby present a study of 3D Fe and Ni relative distributions as well as porosity and permeability of a whole E-cat FCC particle using full-field transmission hard X-ray microscopy (TXM). This technique allows for noninvasive, high-resolution investigation of 3D microstructure and porosity.[10] By providing sub-30 nm 2D resolution,[11] TXM is able to visualize macroporosity (pores with diameters above 50 nm). By stitching together multiple fields of view (FOVs) the 30 × 30 μm^2 FOV can be extended to form a large mosaic image at every angle of a tomographic scan to image the entire FCC particle in 3D.[12] Three-dimensional relative elemental distributions of Fe and Ni can be generated using differential contrast,[13] allowing for an investigation of the effects of metal poisoning. Further details on the sample preparation and experimental details can be found in the Supporting Information.

The reconstructed tomography data recorded for the total FCC particle (Figure 1) shows nodules and valleys on the surface, causing a mottled shape. The relative Fe and Ni distributions within the FCC particle are shown in Figure 1b–d, where the Fe distribution is indicated by a red to yellow color scale, and Ni is indicated by a blue to green color scale, where yellow and green represent larger relative elemental concentrations.

Comparing the optical density from tomography data collected at 7060 eV (below the Fe and Ni K absorption edges) with the relative elemental distributions, we notice that the nodules of the FCC particle mainly coincide with areas of larger metal contamination. This correlation is visualized more

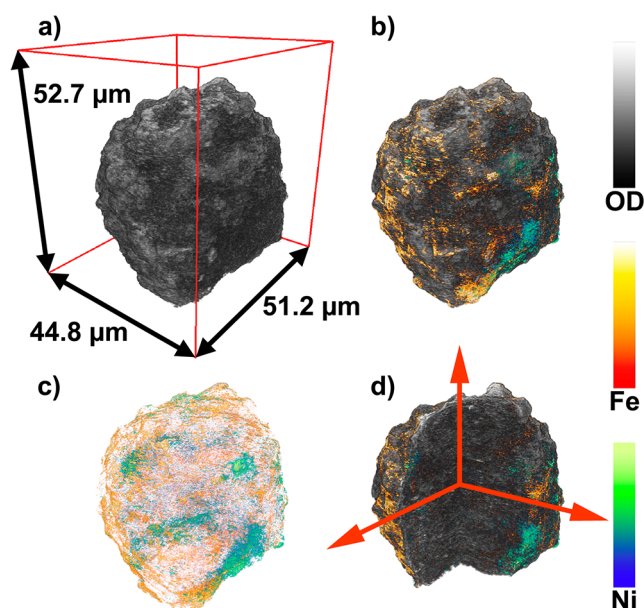**Figure 1.** Three-dimensional representation of a ~50 μm diameter FCC particle based on TXM mosaic computed tomography with a voxel size of 64 × 64 × 64 nm³. (a) Optical density (OD) as recorded at 7060 eV. (b–d) Visualization of Fe (orange) and Ni (blue) 3D relative distributions obtained from differences of tomography data: 7160−7060 and 8400−8300 eV, respectively. (d) Cut-through of the tomography data showing the inner structure of the particle.

clearly in Figure 2, showing a slice in the *xz* plane through the FCC particle comparing optical density at 7060 eV with Fe and Ni distributions. Yaluris et al. have suggested that when metals interact with binder in FCC particles, the melting points of the
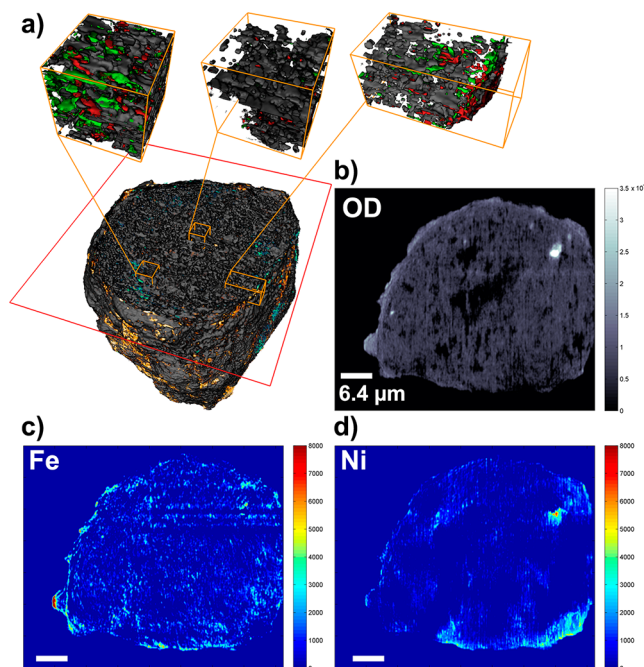

Figure 2. Relative Fe and Ni distributions within the FCC particle. (a) Cut through the reconstructed FCC particle and selected subvolumes showing the 3D distribution of particle matrix (dark gray), Fe (red), and Ni (green). (b–d) Slices in the *xz* plane of the reconstructed volume displaying (b) the optical density at 7060 eV, (c) relative Fe distribution, and (d) relative Ni distribution.

Si-rich phases are lowered substantially.[14] In the high-temperature FCC unit, vitrification occurs in which low melting point phases (Si-rich areas) cause the particle structure to collapse around high-melting point phases (Al-rich areas), causing nodules and valleys to form.[14] The slices through the tomographic data show a denser surface crust and some accumulation of Fe in highly localized areas ("hot spots") within the particle and in nodules and valleys (Figure 2b), indicated by the contour along the outer edges. Finding Fe "hot spots" is not surprising as Fe is present not only in the feedstock but is a constituent in the clay component of the FCC particle. The largest Ni concentrations are mainly confined to the outer regions of the particle. Figure 2a visualizes these observations by displaying a subvolume at the surface (rightmost), a region with enriched metal concentration ("hot spot", left), and a central subvolume containing little Fe and Ni (center).

We also determined the radial dependence of the heterogeneity of Fe and Ni distributions within the catalyst (Figure 3a) by comparing relative metal concentration with the
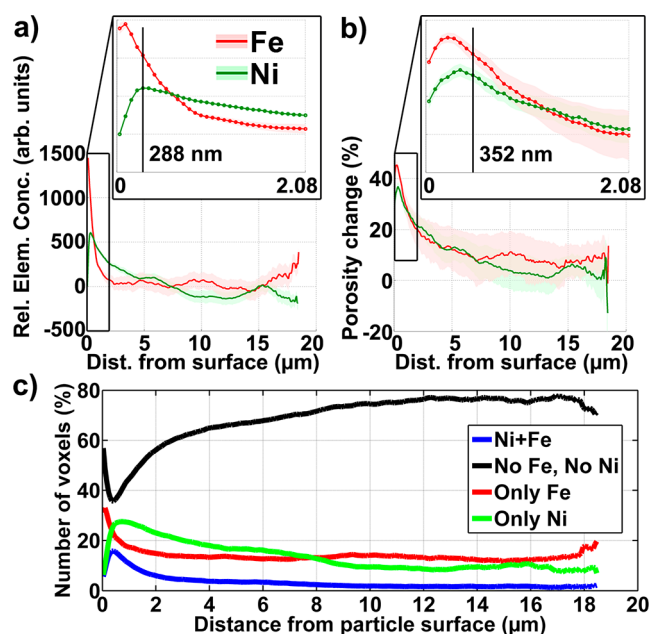

Figure 3. Relative Fe and Ni distributions plotted as a function of distance from the FCC particle surface (a), and related porosity changes caused by the presence of these metals (b). The insets show a zoom of the near-surface region. The vertical lines indicate the distances of the 5th and 6th concentric shells (single voxel thickness) formed by voxels with identical distance to the particle surface. (c) Correlation of relative Fe and Ni concentrations, shown by plotting the number of voxels in each shell that contain both Ni and Fe (blue), only Fe (red), only Ni (green), or none of those metals (black). Numbers have been normalized to percent, where 100% indicates all voxels of each 64 nm thick shell.

smallest distance of each voxel to the outer particle surface. In this way we can account for the irregular shape of the particle and nodules and valleys at the surface, and were able to plot the relative Fe and Ni concentrations as a function of distance from the particle surface. Voxels with identical distances were pooled, forming concentric shells of single voxel thickness (64 nm), and the relative elemental concentrations for each shell were then calculated as the average for all those voxels. Furthermore, the porosity of each shell was determined as the ratio of void space

(volume of voxels in the shell assigned to pore space) to the total volume of all voxels in the shell. This allowed us to correlate changes in porosity with the presence or absence of Fe and/or Ni.

The resulting plots (Figure 3) clearly show that Fe and Ni mainly accumulate at and near the surface of the particle, which indicates that both metals have been incorporated during the FCC process, entering the particle from the surface. While Fe concentrations are largest within 1 μm from the surface, suggesting a surface deposition mechanism, Ni penetrates deeper into the particle with a peak concentration at about 300 nm and significant concentration levels up to 3−4 μm. Beyond about 4 μm into the particle, both Fe and Ni relative concentrations become small, approaching the detection limit of the method. In the interior of the particle, Fe relative concentrations are dominated by the presence of Fe "hot spots" in the particle matrix, while relative Ni concentrations fall below 0 beyond about 7 μm into the particle. Negative values are expected for relative concentration mapping because the elemental concentrations are calculated as the difference between data collected above and below the X-ray absorption edge, which results in negative differential absorption values if no metal is present. This is because the X-ray absorption coefficient decreases with increasing X-ray energy in the absence of an absorber specific to the X-ray energy. The negative Ni concentrations therefore indicate that Ni contaminants have reached an average depth of about 7 μm in this particle.

To assess the effect of Fe and Ni contaminants on the particle's pore space, we investigated the porosity change due to their presence. This was achieved by comparing the pore space established below the X-ray absorption edge of each metal with the (reduced) pore space above the edge. Any detected change in porosity can then be attributed to the presence of the metal clogging the macropore space. Figure 3b shows a clear correlation between the determined porosity change and the relative elemental concentrations, indicating that those metals are indeed clogging macropore space. The largest porosity changes coincide with the maxima of elemental concentrations, indicating that the strongest macropore clogging effects happen within the first 1−2 μm, i.e., the surface of the particle.

Since concentrations as well as porosity changes caused by both Fe and Ni are confined to the surface layer of the particle we inspected the spatial correlation of the two metals[13] because a high spatial correlation would indicate a similar incorporation mechanism. Figure 3c shows the correlation plot of Fe and Ni as a function of the distance from the particle surface. Voxels of each class (pure Fe, pure Ni, mixture of Fe and Ni, and no metal) and with identical distances were counted, and the counts normalized to the total number of voxels in each shell to account for the decreasing shell size when going deeper into the particle. Interestingly, voxels containing both metals, indicating spatially correlated Fe and Ni, are always found in significantly smaller fractions than voxels containing pure metal concentrations. This is another strong indication that the incorporation mechanisms for Fe and Ni are different, and we believe that this is due to a different mobility of the respective metal transporting species.

Finally we also investigated the accessibility of the FCC particle and how it relates to the presence of Fe and Ni by performing permeability measurements for two selected subvolumes in the particle (see Supporting Information for details about the permeability calculation). By overlaying the calculated relative mass flow velocity vector field through the macropores with the 3D metal distribution maps, we obtained a picture of the effects of Fe and Ni contamination. Figure 4
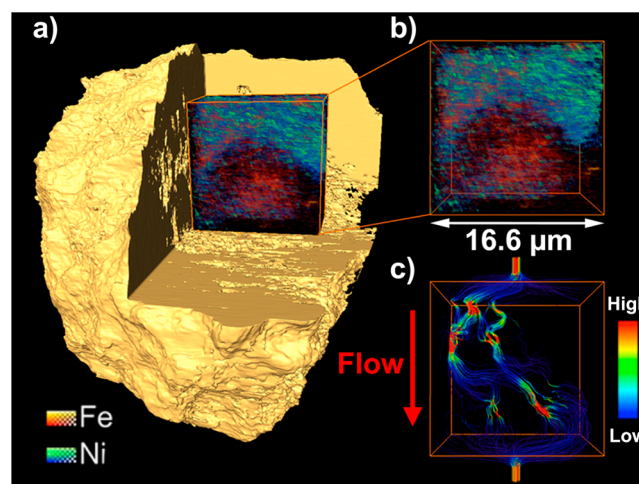

Figure 4. Permeability calculation for a subvolume: (a,b) a subregion (16.6 × 16.6 × 10.0 μm^3) of the pore space is selected, considering relative Fe and Ni distributions. (c) After the permeability experiment, mass transport through the subvolume along the selected axis (red arrow) is visualized using the velocity field of the fluid. The streamlines indicate the magnitude of the velocity field where red represents the highest velocity (i.e., where pore space constriction is greatest) and blue colors indicate lowest velocities.

shows the results obtained for a representative subvolume (16.6 × 16.6 × 10.0 μm^3), which includes near-surface regions as well as more central parts. The subvolume does not include the part of the surface region where the influence of Fe is strongest (<1 μm from the surface); this was done to inspect the zone of the FCC particle where the influence of Fe and Ni starts to become negligible, i.e., around 4 μm into the particle (see Figure 3). Typical for deeper regions of the particle (>∼2 μm), Fe is found in lower concentrations and throughout the subvolume as part of the particle matrix, while the Ni distribution is more heterogeneous, being found predominantly at the top of the subvolume, i.e., closer to the surface. The subvolume's pore space determined at 7060 eV and reduced by the pore clogging effect of Fe and Ni was then used to perform a permeability calculation resulting in a velocity field as visualized by the colored streamlines. Examining the fluid flow through the subvolume reveals two effects: First, we observed constriction of fluid flow where Ni is present, indicated by the high velocity (red area) fluid flow through small cross sectional areas. Elsewhere in the region, with little to no Ni, flow is less inhibited (blue streamlines). Second we observed inaccessibility of areas with large Ni content because the Ni contamination is clogging some macropores completely. These qualitative observations are in good agreement with the radial evaluation reported earlier and visualize the pore clogging effects of the metal.

In conclusion, we developed a method for investigating morphology and heavy metal poisoning of individual catalyst particles using full-field X-ray nanotomography. We observed nodules and valleys at the surface of the FCC particle, similar to those seen in surface topography studies of E-cat samples. Fe was distributed along these nodules and valleys, showing largest concentrations within the first 1 μm from the particle surface.

In deeper regions Fe is relatively uniformly distributed throughout the FCC particle except for high concentration "hot spots", due to its natural occurrence in the particle matrix. Ni contaminations were also found confined to the near-surface regions of the catalyst but seem to penetrate deeper into the particle (up to ∼7 μm from the surface). The correlation of relative elemental concentrations with porosity changes as a function of distance from the particle surface has shown that both Fe and Ni contaminate the particle from the outside where the oil feedstock enters the particle. On the basis of these promising results, further investigations of fresh and E-cat samples will be performed to fully examine the effects of metal contamination on FCC particles.

■ ASSOCIATED CONTENT

ⓢ Supporting Information
Sample preparation, reconstruction protocol, radial calculations, and permability calculations. This material is available free of charge via the Internet at http://pubs.acs.org.

■ AUTHOR INFORMATION

Corresponding Authors
*b.m.weckhuysen@uu.nl
*jandrewshayter@gmail.com

Author Contributions
§These authors contributed equally to this work.

Notes
The authors declare no competing financial interest.

■ ACKNOWLEDGMENTS

■ REFERENCES

(1) Sadeghbeigi, R. *Fluid Catalytic Cracking Handbook: an Expert Guide to the Practical Operation, Design, and Optimization of Fcc Units*, 3rd ed.; Butterworth-Heinemann: Oxford, U.K., 2012.

(2) Bayraktar, O.; Kugler, E. *Catal. Lett.* **2003**, *90*, 155−160.

(3) Grunwaldt, J.-D.; Wagner, J. B.; Dunin-Borkowski, R. E. *ChemCatChem* **2013**, *5*, 62−80.

(4) Bayraktar, O.; Kugler, E. L. *Catal. Lett.* **2003**, *90*, 155−160.

(5) Chao, K. J.; Lin, L. H.; Ling, Y. C.; Hwang, J. F.; Hou, L. Y. *Appl. Catal., A* **1995**, *121*, 217−229.

(6) Psarras, A. C.; Iliopoulou, E. F.; Nalbandian, L.; Lappas, A. A.; Pouwels, C. *Catal. Today* **2007**, *127*, 44−53.

(7) Buurmans, I. L. C.; Ruiz-Martínez, J.; Knowles, W. V.; van der Beek, D.; Bergwerff, J. A.; Vogt, E. T. C.; Weckhuysen, B. M. *Nat. Chem.* **2011**, *3*, 862−867.

(8) Karreman, M. A.; Buurmans, I. L. C.; Geus, J. W.; Agronskaia, A. V.; Ruiz-Martínez, J.; Gerritsen, H. C.; Weckhuysen, B. M. *Angew. Chem., Int. Ed.* **2012**, *51*, 1428−1431.

(9) Bare, S. R.; Charochak, M. E.; Kelly, S. D.; Lai, B.; Wang, J.; Chen-Wiegart, Y. K. *ChemCatChem* **2014**, *6*, 1427−1437.

(10) (a) Shearing, P. R.; Brandon, N. P.; Gelb, J.; Bradley, R.; Withers, P. J.; Marquis, A. J.; Cooper, S.; Harris, S. *J. Electrochem. Soc.* **2012**, *159*, A1023−A1027. (b) Nelson, G. J.; Harris, W. M.; Lombardo, J. J.; Izzo, J. R., Jr.; Chiu, W. K. S.; Tanasini, P.; Cantoni, M.; van Herle, J.; Comninellis, C.; Andrews, J. C.; Liu, Y.; Pianetta, P.; Chu, Y. S. *Electrochem. Commun.* **2011**, *13*, 586−589. (c) Chen-Wiegart, Y. K.; Cronin, J. S.; Yuan, Q.; Yakal-Kremski, K. J.; Barnett, S. A.; Wang, J. *J. Power Sources* **2012**, *218*, 348−351.

(11) Liu, Y.; Andrews, J. C.; Wang, J.; Meirer, F.; Zhu, P.; Wu, Z.; Pianetta, P. *Opt. Express* **2011**, *19*, 540−545.

(12) Liu, Y.; Meirer, F.; Williams, P. A.; Wang, J.; Andrews, J. C.; Pianetta, P. *J. Synchrotron Rad.* **2012**, *19*, 281−287.

(13) Kao, T. L.; Shi, C. Y.; Wang, J.; Mao, W. L.; Liu, Y.; Yang, W. *Microsc. Res. Technol.* **2013**, *76*, 1112−1117.

(14) Yaluris, G.; Cheng, W.-C.; Peters, M.; McDowell, L. T.; Hunt, L. Mechanism of Fluid Cracking Catalysts Deactivation by Fe. In *Studies in Surface Science and Catalysis*; Occelli, M., Ed.; Elsevier B.V.: New York, 2004; pp 139−163.